Renewable Energy and Power Quality Journal
https://repqj.com/index.php/repqj/index
RE&PQJ, Vol. 24, No. 5, 2026

# Transient Current Response Modeling and Voltage Analysis of Three-Phase PWM Inverter Systems Considering Parasitic Parameters and Passive EMI Filter Effects

YunHo Pak, JuSong Kim, YongSim Ro, JinHyok Ri*

Faculty of Electrical Engineering, Kim Chaek University of Technology, Pyongyang, Democratic People's Republic of Korea

*Corresponding Author: JinHyok Ri, rjh19870919@163.com

**Article History**

Received: 14 September 2026 Revised: 30 September 2026

Accepted: 03 November 2026 Available Online: 24 November 2026

**Abstract.** High-frequency switching in pulse-width-modulated (PWM) inverter systems for renewable energy applications produces steep voltage impulses and current transients that excite parasitic current paths, increase common-mode and differential-mode electromagnetic interference (EMI), and degrade power quality in inverter-fed motor drives. This paper develops a transient current-response model for a three-phase PWM inverter by explicitly considering the load impedance, parasitic capacitance associated with the inverter heat sink and motor structure, and the dynamics of a passive inductor-capacitor (LC) output filter For the load-only and parasitic-capacitance cases, analytical current responses are derived in the Laplace domain for a trapezoidal switching-voltage impulse whose rising, on-state, falling, and post-pulse intervals are treated separately. When the LC filter is included, a state-space formulation is adopted and solved numerically by a fourth-order Runge-Kutta procedure with a time step of 0.1 μs. The model is evaluated for a 380-V, 139-A, 60-Hz, 75-kW induction motor supplied by a 130-kVA inverter with a 2.4-kHz carrier frequency. The calculated heat-sink-related parasitic capacitance is 394.93 pF. Comparative MATLAB simulations show that filter parameters strongly influence inverter output current, filter-capacitor voltage, load-current distortion, and overall power quality. The case $L = 2$ mH and $C = 50$ μF provides the smoothest waveforms and the lowest simulated load-current total harmonic distortion (THD = 2.3%) among the investigated configurations, whereas an inadequately selected filter can increase high-frequency current stress and worsen power quality. The proposed framework provides a simulation-based screening tool for passive filter parameters. Experimental validation, including filter-capacitor voltage, load-current, and full electromagnetic compatibility (EMC) measurements, remains necessary and is identified as future work.

**Key words.** Three-phase PWM inverter, Transient current response, Voltage impulse, Passive EMI filter, Parasitic capacitance, State-space model, Leakage current, Motor drive

## 1. Introduction

Three-phase voltage-source PWM inverters are the backbone of modern industrial motor drives, offering precise control of induction and permanent-magnet machines. Their high-frequency switching, however, generates steep du/dt and di/dt transients that energize parasitic capacitances and inductances across the inverter, cable, motor windings, heat sink, and grounding network. The resulting common-mode and differential-mode currents are well-known sources of bearing-current damage, shaft-voltage stress, and conducted or radiated electromagnetic interference [1]. Early modeling efforts by Ogasawara and Akagi laid the groundwork for understanding these leakage-current paths [2], while Wang later demonstrated how shaft voltages and bearing currents develop in medium-voltage drives [3].

The adoption of wide-bandgap semiconductors has intensified these challenges. Faster switching edges improve efficiency and power density but also broaden the noise spectrum and strengthen the coupling between the semiconductor package, heat sink, motor, and filter parasitics [4]. In response, passive and hybrid output filters have become the standard mitigation approach for reducing motor-terminal dv/dt, common-mode current, shaft voltage, and leakage current [5,6]. Passive EMI

filters have proven particularly effective against high-frequency leakage currents [7], while hybrid topologies offer improved common-mode voltage compensation [8]. More recent efforts have explored reduced-common-mode PWM strategies [9], transformerless active EMI filters [10], integrated common-mode filters for wide-bandgap power modules [11,12], active dv/dt filtering [13], and distributed passive cancellation on both input and output sides [14]. A common thread across these studies is that filter performance depends critically on how source impedance, parasitic elements, and filter placement interact [15,16].

Recent reviews have further consolidated these findings, covering EMI suppression in SiC-based drives [17] and active common-mode filter design for wide-bandgap inverters [18]. These works highlight that the dominant interference paths in SiC traction inverters span the gate loop, isolation interface, and inverter/powertrain terminals, and that mitigation techniques must be evaluated together with operating conditions, volume, and integration constraints [17]. These findings are further supported by recent work on EMI filter integration for GaN power modules [19] and passive filters for mitigating neutral-point voltage stress [20].

Despite this progress, practical filter design still relies heavily on frequency-domain attenuation targets or repeated simulation and experimental tuning. Such approaches obscure the time-domain mechanism by which a single switching-voltage impulse produces current stress in the load, excites the parasitic capacitance, and propagates through the filter branches. This work addresses that gap by formulating a current-response model that begins from the switching impulse itself and progressively introduces the dominant physical elements of a three-phase inverter system.

The main contributions of this paper are as follows. First, an analytical transient-current model is derived for a symmetrical three-phase inverter load excited by a trapezoidal voltage impulse. Second, the model is extended to include the parasitic capacitance between the switching-device/heat-sink structure and ground. Third, an LC-filtered system is formulated in state-space form and solved with a fourth-order Runge-Kutta algorithm. Finally, the model is applied to a 75-kW induction-motor drive, and several LC parameter combinations are compared to identify their influence on inverter output current, capacitor voltage, and load-current quality. These contributions provide a physics-based foundation for screening passive filter parameters.

## 2. Transient Current-Response Model Considering the Load Impedance

The switching-voltage waveform is characterized by a rise time $t_r = 0.1$ μs, an on-state duration $t_{on}$, a fall time $t_f = 0.1$ μs and a peak amplitude $U_D$ (in the numerical study) (Table 1).

**Table 1.** Nomenclature.

| Symbol | Definition |
|---|---|
| $U_D$ | DC-link voltage |
| $t_r$, $t_{on}$, $t_f$ | Rise, on-state, fall times |
| $R_0$, $L_0$ | Equivalent load resistance and inductance |
| $C_T$ | Heat-sink parasitic capacitance per switch |
| $C_p$ | Equivalent parasitic capacitance per phase leg |
| $C_G$ | Stator-to-frame capacitance |
| $L$, $C$ | Filter inductance and capacitance |
| $i_L$ | Filter inductor current |
| $u_C$ | Filter capacitor voltage |
| $i_2$ | Load current |
| $f_{sw}$ | Switching frequency (2.4 kHz) |

Figure 1 shows the three-phase PWM inverter and the balanced load considered in the first stage of the analysis. To isolate the fundamental transient mechanism, the three phases are assumed to be symmetrical and the switching event in one phase is represented by an ideal trapezoidal voltage impulse.

The equivalent single-phase circuit and the applied trapezoidal voltage impulse are shown in Figure 2, where $R_0$ and $L_0$ denote the equivalent total resistance and inductance of the load, respectively.

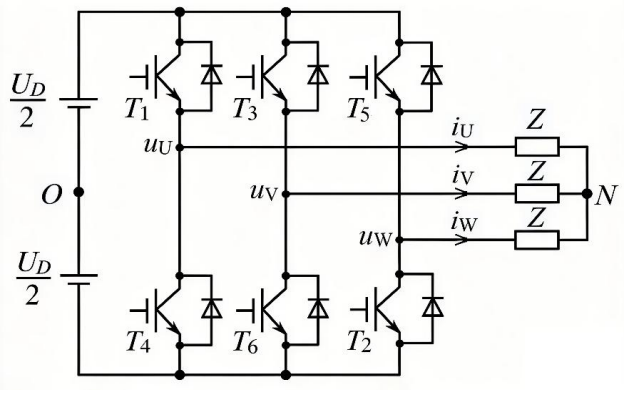


**Figure 1**. Three-phase PWM voltage-source inverter with a balanced load.

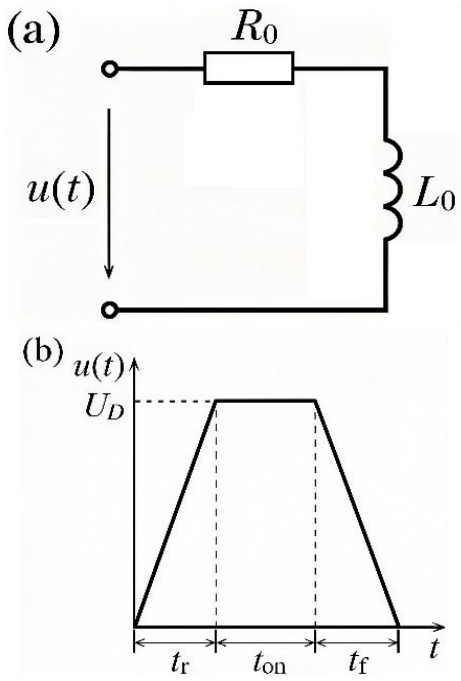


**Figure 2**. Per-phase equivalent R-L circuit and idealized trapezoidal voltage impulse. (a) Equivalent circuit, (b) Voltage impulse waveform.

For the equivalent *R-L* branch, the current-to-voltage transfer function in the Laplace domain is given by

$$H_Y(S)=\frac{I(S)}{U(S)}=\frac{1}{R_0+SL_0} \quad (1)$$

The corresponding impulse response is obtained by inverse Laplace transformation as

$$h(t)=L^{-1}[H_Y(S)]=\frac{1}{L_0}e^{-\frac{R_0}{L_0}t} \quad (2)$$

For the trapezoidal excitation in Figure 2(b), the current is evaluated piecewise over four consecutive time intervals. This piecewise formulation preserves the finite switching rise and fall times rather than replacing the switching event by an ideal step.

$$i(t)=\int_0^t u(\tau)h(t-\tau)\mathrm{d}\tau=\int_0^t u(\tau)\frac{1}{L_0}e^{-\frac{R_0}{L_0}t}e^{\frac{R_0}{L_0}\tau}\mathrm{d}\tau \quad (3)$$

Equations 4-7 give the analytical expressions for the rising ( $0<t<t_r$ ), constant-voltage ( $t_r<t<t_r+t_{on}$ ), falling ( $t_r+t_{on}<t<t_r+t_{on}+t_f$ ), and post-pulse ( $t>t_r+t_{on}+t_f$ ) intervals, respectively.

$$i(t)=\int_0^t u(\tau)h(t-\tau)\mathrm{d}\tau=\int_0^t u(\tau)\frac{1}{L_0}e^{-\frac{R_0}{L_0}t}e^{\frac{R_0}{L_0}\tau}\mathrm{d}\tau \quad (4)$$

$$\begin{aligned} i(t)&=\frac{U_D}{R_0t_r}\left(\frac{L_0}{R_0}e^{-\frac{R_0}{L_0}t}+t-\frac{L_0}{R_0}\right)-\frac{U_D}{R_0t_r}\left(\frac{L_0}{R_0}e^{-\frac{R_0}{L_0}(t-t_r)}+t-t_r-\frac{L_0}{R_0}\right)\\ &=\frac{U_D}{R_0t_r}\left[\frac{L_0}{R_0}e^{-\frac{R_0}{L_0}t}\left(1-e^{\frac{R_0}{L_0}t_r}\right)+t_r\right] \end{aligned} \quad (5)$$

$$\begin{aligned} i(t)&=\frac{U_D}{R_0t_r}\left(\frac{L_0}{R_0}e^{-\frac{L_0}{R_0}t}\left(1-e^{\frac{L_0}{R_0}t_r}\right)+t_r\right)-\frac{U_D}{R_0t_r}\left(\frac{L_0}{R_0}e^{-\frac{L_0}{R_0}(t-t_r-t_{on})}+t-t_r-t_{on}-\frac{L_0}{R_0}\right)\\ &=\frac{U_D}{R_0t_r}\left[\frac{L_0}{R_0}e^{-\frac{R_0}{L_0}t}\left(1-e^{\frac{R_0}{L_0}t_r}-e^{\frac{R_0}{L_0}(t_r+t_{on})}\right)-t+2t_r+t_{on}+\frac{L_0}{R_0}\right] \end{aligned} \quad (6)$$

$$\begin{aligned} i(t)&=\frac{U_D}{R_0t_r}\left(\frac{L_0}{R_0}e^{-\frac{L_0}{R_0}t}\left(1-e^{\frac{L_0}{R_0}t_r}-e^{\frac{L_0}{R_0}(t_r+t_{on})}\right)-t+2t_r+t_{on}+\frac{L_0}{R_0}\right)+\frac{U_D}{R_0t_r}\left(\frac{L_0}{R_0}e^{-\frac{L_0}{R_0}(t-t_r-t_{on}-t_f)}+t-t_r-t_{on}-t_f-\frac{L_0}{R_0}\right)\\ &=\frac{U_D}{R_0t_r}\left[\frac{L_0}{R_0}e^{-\frac{R_0}{L_0}t}\left(1-e^{\frac{R_0}{L_0}t_r}-e^{\frac{R_0}{L_0}(t_r+t_{on})}+e^{\frac{R_0}{L_0}(t_r+t_{on}+t_f)}\right)t_r-t_f\right] \end{aligned} \quad (7)$$

## 3. Current-Response Model Including Heat-Sink Parasitic Capacitance

The second stage of the model introduces the dominant capacitive paths associated with the inverter structure. Figure 3 shows the three-phase inverter including the parasitic capacitances between the switching-device/heat -sink structure and ground, together with the load branch. Each IGBT is represented with its individual parasitic capacitance $C_{\mathrm{T}}$ to the grounded heat sink. Because the three phase legs are switched 120° apart, the six IGBT-heat-sink interfaces do not couple simultaneously; their time-averaged effect can be lumped into a single equivalent capacitance $C_{\mathrm{p}}$ for one phase leg. In this reduced circuit, $C_{\mathrm{p}}$ provides a parallel path to ground, while the load branch $(R_0 - L_0)$ carries the differential-mode current. The total current is therefore decomposed into two components.

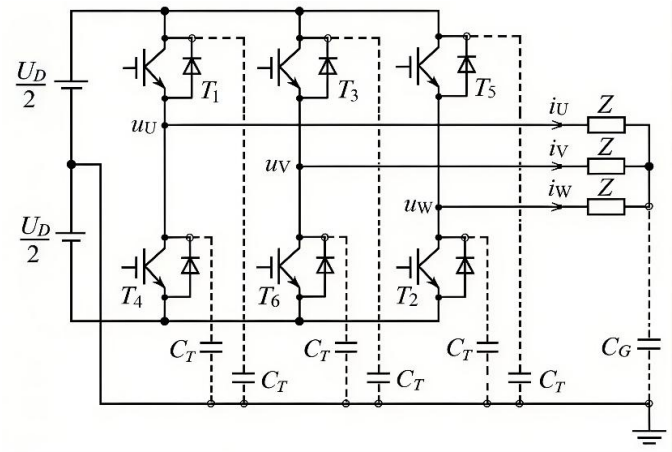


**Figure 3**. Three-phase inverter model with per-IGBT heat-sink parasitic capacitances $C_{\mathrm{T}}$ and stator-to-frame capacitance $C_{\mathrm{G}}$.

In Figure 3, $C_{\mathrm{T}}$ represents the equivalent parasitic capacitance associated with the switching-device/heat-sink path, while $C_{\mathrm{G}}$ denotes the capacitance between the stator winding and the grounded motor frame. These capacitances provide high-frequency return paths and therefore influence the magnitude and shape of the switching-induced current.

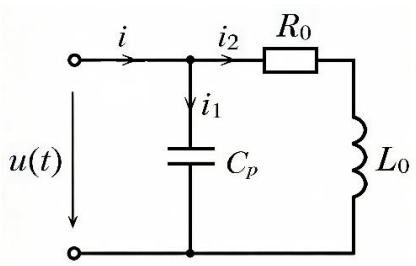


**Figure 4**. Per-phase equivalent circuit with the lumped heat-sink parasitic capacitance $C_{\mathrm{p}}$.

Figure 4 isolates the heat-sink parasitic branch in order to derive its transient response. The stator-to-frame capacitance is omitted from this reduced equivalent circuit so that the individual branch contributions can be identified explicitly. The lumped capacitance $C_{\mathrm{p}}$ in Figure 4 is related to the per-device capacitance $C_{\mathrm{T}}$ in Figure 3 through the three-phase switching symmetry, as will be quantified in Section 5.

In the Laplace domain, the total current is decomposed into the current through the parasitic capacitive branch and the current through the $R_0 - L_0$ load branch. The corresponding transfer functions are given by equation 8.

$$\begin{cases} H_Y(S) = \dfrac{I(S)}{U(S)} = \dfrac{1}{R_{C_{\mathrm{p}}} + \dfrac{1}{SC_{\mathrm{p}}}} + \dfrac{1}{R_0 + SL_0} \\ H_{1Y}(S) = \dfrac{1}{R_{C_{\mathrm{p}}} + \dfrac{1}{SC_{\mathrm{p}}}} = \dfrac{1}{R_{C_{\mathrm{p}}}} \left( 1 - \dfrac{1}{R_{C_{\mathrm{p}}} C_{\mathrm{p}}} \cdot \dfrac{1}{S + \dfrac{1}{R_{C_{\mathrm{p}}} C_{\mathrm{p}}}} \right) \\ H_{2Y}(S) = \dfrac{1}{R_0 + SL_0} \end{cases} \tag{8}$$

Inverse Laplace transformation of the transfer functions yields the impulse responses of the complete branch, the parasitic-capacitance branch, and the load branch, as expressed by equation 9.

$$\begin{cases} h(t) = L^{-1}\left[H_Y(S)\right] = \dfrac{1}{R_{C_{\mathrm{p}}}} \cdot \delta(t) - \dfrac{1}{R_{C_{\mathrm{p}}}^2 C_{\mathrm{p}}} e^{-\frac{t}{R_{C_{\mathrm{p}}} C_{\mathrm{p}}}} + \dfrac{1}{L_0} e^{-\frac{R_0}{L_0} t} \\ h_1(t) = L^{-1}\left[H_{1Y}(S)\right] = \dfrac{1}{R_{C_{\mathrm{p}}}} \cdot \delta(t) - \dfrac{1}{R_{C_{\mathrm{p}}}^2 C_{\mathrm{p}}} e^{-\frac{t}{R_{C_{\mathrm{p}}} C_{\mathrm{p}}}} \\ h_2(t) = L^{-1}\left[H_{2Y}(S)\right] = \dfrac{1}{L_0} e^{-\frac{R_0}{L_0} t} \end{cases} \tag{9}$$

The time-domain currents are obtained by convolving the voltage impulse with the corresponding impulse responses, as given by equation 10.

$$\begin{cases} i(t)=\int_0^t h(t-\tau)\mathrm{d}\tau=\int_0^t u(\tau)\left[\dfrac{1}{R_{C_\mathrm{p}}}\cdot\delta(t-\tau)-\dfrac{1}{R_{C_\mathrm{p}}^2C_\mathrm{p}}e^{-\frac{1}{R_{C_\mathrm{p}}C_\mathrm{p}}(t-\tau)}+\dfrac{1}{L_0}e^{-\frac{R_0}{L_0}(t-\tau)}\right]\mathrm{d}\tau \\ i_1(t)=\int_0^t u(\tau)h_1(t-\tau)\mathrm{d}\tau=\int_0^t u(\tau)\left[\dfrac{1}{R_{C_\mathrm{p}}}\cdot\delta(t-\tau)-\dfrac{1}{R_{C_\mathrm{p}}^2C_\mathrm{p}}e^{-\frac{1}{R_{C_\mathrm{p}}C_\mathrm{p}}(t-\tau)}\right]\mathrm{d}\tau \\ i_2(t)=\int_0^t u(\tau)h_2(t-\tau)\mathrm{d}\tau=\int_0^t u(\tau)\dfrac{1}{L_0}e^{-\frac{R_0}{L_0}(t-\tau)}\mathrm{d}\tau \end{cases} \tag{10}$$

As in Section 2, the finite trapezoidal switching waveform is evaluated over four time intervals. The parasitic-branch, load-branch, and total currents for each interval ( $0<t<t_\mathrm{r}$ , $t_\mathrm{r}<t<t_\mathrm{r}+t_\mathrm{on}$ , $t_\mathrm{r}+t_\mathrm{on}<t<t_\mathrm{r}+t_\mathrm{on}+t_\mathrm{f}$ , and $t>t_\mathrm{r}+t_\mathrm{on}+t_\mathrm{f}$ ) are given by equations 11-14.

$$\begin{cases} i_1(t)=\int_0^t \dfrac{U_\mathrm{D}}{t_\mathrm{r}}\tau\cdot\left[\dfrac{1}{R_C}\cdot\delta(t-\tau)-\dfrac{1}{R_C^2C}e^{-\frac{1}{R_{C_\mathrm{p}}C_\mathrm{p}}(t-\tau)}\right]\mathrm{d}\tau \\ \quad=\dfrac{U_\mathrm{D}}{t_\mathrm{r}R_{C_\mathrm{p}}}\left[\int_0^t\tau\cdot\delta(t-\tau)\mathrm{d}\tau-\int_0^t\dfrac{1}{R_{C_\mathrm{p}}C_\mathrm{p}}\tau\cdot e^{-\frac{1}{R_{C_\mathrm{p}}C_\mathrm{p}}(t-\tau)}\mathrm{d}\tau\right] \\ \quad=-\dfrac{U_\mathrm{D}}{t_\mathrm{r}R_{C_\mathrm{p}}}\left(R_{C_\mathrm{p}}C_\mathrm{p}\cdot e^{-\frac{t}{R_{C_\mathrm{p}}C_\mathrm{p}}}+t-R_{C_\mathrm{p}}C_\mathrm{p}\right) \\ i_2(t)=\dfrac{U_\mathrm{D}}{R_0t_\mathrm{r}}\left(\dfrac{L_0}{R_0}e^{-\frac{R_0}{L_0}t}+t-\dfrac{L_0}{R_0}\right) \\ i(t)=-\dfrac{U_\mathrm{D}}{t_\mathrm{r}R_{C_\mathrm{p}}}\left(R_{C_\mathrm{p}}C\cdot e^{-\frac{t}{R_{C_\mathrm{p}}C_\mathrm{p}}}+t-R_{C_\mathrm{p}}C_\mathrm{p}\right)+\dfrac{U_\mathrm{D}}{R_0t_\mathrm{r}}\left[\dfrac{L_0}{R_0}e^{-\frac{R_0}{L_0}t}\left(1-e^{\frac{R_0}{L_0}t_\mathrm{r}}\right)+t_\mathrm{r}\right] \end{cases} \tag{11}$$

$$\begin{cases} i_1(t)=-\dfrac{U_\mathrm{D}}{t_\mathrm{r}R_{C_\mathrm{p}}}\left(R_{C_\mathrm{p}}C_\mathrm{p}\cdot e^{-\frac{t}{R_{C_\mathrm{p}}C_\mathrm{p}}}+t-R_{C_\mathrm{p}}C_\mathrm{p}\right)+\dfrac{U_\mathrm{D}}{t_\mathrm{r}R_C}\left(R_{C_\mathrm{p}}C_\mathrm{p}\cdot e^{-\frac{t}{R_{C_\mathrm{p}}C_\mathrm{p}}}\cdot e^{\frac{t_\mathrm{r}}{R_{C_\mathrm{p}}C_\mathrm{p}}}+t-R_{C_\mathrm{p}}C_\mathrm{p}\right) \\ \quad=\dfrac{U_\mathrm{D}}{t_\mathrm{r}R_{C_\mathrm{p}}}\left[R_{C_\mathrm{p}}C_\mathrm{p}\cdot e^{-\frac{t}{R_{C_\mathrm{p}}C_\mathrm{p}}}\left(e^{\frac{t_\mathrm{r}}{R_{C_\mathrm{p}}C_\mathrm{p}}}-1\right)-t_\mathrm{r}\right] \\ i_2(t)=\dfrac{U_\mathrm{D}}{R_0t_\mathrm{r}}\left[\dfrac{L_0}{R_0}e^{-\frac{R_0}{L_0}t}\left(1-e^{\frac{R_0}{L_0}t_\mathrm{r}}\right)+t_\mathrm{r}\right] \\ i(t)=\dfrac{U_\mathrm{D}}{t_\mathrm{r}R_{C_\mathrm{p}}}\left[R_{C_\mathrm{p}}C_\mathrm{p}\cdot e^{-\frac{t}{R_{C_\mathrm{p}}C_\mathrm{p}}}\left(e^{\frac{t_\mathrm{r}}{R_{C_\mathrm{p}}C_\mathrm{p}}}-1\right)-t_\mathrm{r}\right]+\dfrac{U_\mathrm{D}}{R_0t_\mathrm{r}}\left[\dfrac{L_0}{R_0}e^{-\frac{R_0}{L_0}t}\left(1-e^{\frac{R_0}{L_0}t_\mathrm{r}}\right)+t_\mathrm{r}\right] \end{cases} \tag{12}$$

$$
\begin{cases}
i_1(t)=\dfrac{U_{\mathrm{D}}}{t_{\mathrm{r}}R_{C_{\mathrm{p}}}}R_{C_{\mathrm{p}}}C_{\mathrm{p}}\cdot e^{-\frac{t}{R_{C_{\mathrm{p}}}C_{\mathrm{p}}}}\left(e^{\frac{t_{\mathrm{r}}}{R_{C_{\mathrm{p}}}C_{\mathrm{p}}}}-1\right)+\dfrac{U_{\mathrm{D}}}{t_{\mathrm{r}}R_{C_{\mathrm{p}}}}\left(R_{C_{\mathrm{p}}}C_{\mathrm{p}}\cdot e^{-\frac{t}{R_{C_{\mathrm{p}}}C_{\mathrm{p}}}}\cdot e^{\frac{t_{\mathrm{r}}+t_{\mathrm{on}}}{R_{C_{\mathrm{p}}}C_{\mathrm{p}}}}+t-R_{C_{\mathrm{p}}}C_{\mathrm{p}}\right)\\
\quad=\dfrac{U_{\mathrm{D}}}{t_{\mathrm{r}}R_{C_{\mathrm{p}}}}R_{C_{\mathrm{p}}}C_{\mathrm{p}}\cdot e^{-\frac{t}{R_{C_{\mathrm{p}}}C_{\mathrm{p}}}}\left(e^{\frac{t_{\mathrm{r}}}{R_{C_{\mathrm{p}}}C_{\mathrm{p}}}}-1+e^{\frac{t_{\mathrm{r}}+t_{\mathrm{on}}}{R_{C_{\mathrm{p}}}C_{\mathrm{p}}}}+t-2t_{\mathrm{r}}-t_{\mathrm{on}}-R_{C_{\mathrm{p}}}C_{\mathrm{p}}\right)\\
i_2(t)=\dfrac{U_{\mathrm{D}}}{R_0t_{\mathrm{r}}}\left[\dfrac{L_0}{R_0}e^{-\frac{R_0}{L_0}t}\left(1-e^{\frac{R_0}{L_0}t_{\mathrm{r}}}-e^{\frac{R_0}{L_0}(t_{\mathrm{r}}+t_{\mathrm{on}})}\right)-t+2t_{\mathrm{r}}+t_{\mathrm{on}}+\dfrac{L_0}{R_0}\right]\\
i(t)=\dfrac{U_{\mathrm{D}}}{t_{\mathrm{r}}R_{C_{\mathrm{p}}}}R_{C_{\mathrm{p}}}C_{\mathrm{p}}\cdot e^{-\frac{t}{R_{C_{\mathrm{p}}}C_{\mathrm{p}}}}\left(e^{\frac{t_{\mathrm{r}}}{R_{C_{\mathrm{p}}}C_{\mathrm{p}}}}-1+e^{\frac{t_{\mathrm{r}}+t_{\mathrm{on}}}{R_{C_{\mathrm{p}}}C_{\mathrm{p}}}}+t-2t_{\mathrm{r}}-t_{\mathrm{on}}-R_{C_{\mathrm{p}}}C_{\mathrm{p}}\right)+\\
\quad+\dfrac{U_{\mathrm{D}}}{R_0t_{\mathrm{r}}}\left[\dfrac{L_0}{R_0}e^{-\frac{R_0}{L_0}t}\left(1-e^{\frac{R_0}{L_0}t_{\mathrm{r}}}-e^{\frac{R_0}{L_0}(t_{\mathrm{r}}+t_{\mathrm{on}})}\right)-t+2t_{\mathrm{r}}+t_{\mathrm{on}}+\dfrac{L_0}{R_0}\right]
\end{cases}
\tag{13}
$$

$$
\begin{cases}
i_1(t)=\dfrac{U_{\mathrm{D}}}{t_{\mathrm{r}}R_{C_{\mathrm{p}}}}R_{C_{\mathrm{p}}}C_{\mathrm{p}}\cdot e^{-\frac{t}{R_{C_{\mathrm{p}}}C_{\mathrm{p}}}}\left(e^{\frac{t}{R_{C_{\mathrm{p}}}C_{\mathrm{p}}}}-1+e^{\frac{t_{\mathrm{r}}+t_{\mathrm{on}}}{R_{C_{\mathrm{p}}}C_{\mathrm{p}}}}-R_{C_{\mathrm{p}}}C_{\mathrm{p}}\right)-\dfrac{U_{\mathrm{D}}}{t_{\mathrm{r}}R_{C_{\mathrm{p}}}}\left(R_{C_{\mathrm{p}}}C_{\mathrm{p}}\cdot e^{-\frac{t}{R_{C_{\mathrm{p}}}C_{\mathrm{p}}}}\cdot e^{\frac{t_{\mathrm{r}}+t_{\mathrm{on}}+t_{\mathrm{f}}}{R_{C_{\mathrm{p}}}C_{\mathrm{p}}}}-R_{C_{\mathrm{p}}}C_{\mathrm{p}}\right)\\
\quad=\dfrac{U_{\mathrm{D}}}{t_{\mathrm{r}}R_{C_{\mathrm{p}}}}\left[R_{C_{\mathrm{p}}}C_{\mathrm{p}}\cdot e^{-\frac{t}{R_{C_{\mathrm{p}}}C_{\mathrm{p}}}}\left(e^{\frac{t_{\mathrm{r}}}{R_{C_{\mathrm{p}}}C_{\mathrm{p}}}}-1+e^{\frac{t_{\mathrm{r}}+t_{\mathrm{on}}}{R_{C_{\mathrm{p}}}C_{\mathrm{p}}}}-e^{\frac{t_{\mathrm{r}}+t_{\mathrm{on}}+t_{\mathrm{f}}}{R_{C_{\mathrm{p}}}C_{\mathrm{p}}}}\right)-t_{\mathrm{r}}+t_{\mathrm{f}}\right]\\
i_2(t)=\dfrac{U_{\mathrm{D}}}{R_0t_{\mathrm{r}}}\left[\dfrac{L_0}{R_0}e^{-\frac{R_0}{L_0}t}\left(1-e^{\frac{R_0}{L_0}t_{\mathrm{r}}}-e^{\frac{R_0}{L_0}(t_{\mathrm{r}}+t_{\mathrm{on}})}+e^{\frac{R_0}{L_0}(t_{\mathrm{r}}+t_{\mathrm{on}}+t_{\mathrm{f}})}\right)+t_{\mathrm{r}}-t_{\mathrm{f}}\right]\\
i(t)=\dfrac{U_{\mathrm{D}}}{t_{\mathrm{r}}R_{C_{\mathrm{p}}}}\left[R_{C_{\mathrm{p}}}C_{\mathrm{p}}\cdot e^{-\frac{t}{R_{C_{\mathrm{p}}}C_{\mathrm{p}}}}\left(e^{\frac{t_{\mathrm{r}}}{R_{C_{\mathrm{p}}}C_{\mathrm{p}}}}-1+e^{\frac{t_{\mathrm{r}}+t_{\mathrm{on}}}{R_{C_{\mathrm{p}}}C_{\mathrm{p}}}}-e^{\frac{t_{\mathrm{r}}+t_{\mathrm{on}}+t_{\mathrm{f}}}{R_{C_{\mathrm{p}}}C_{\mathrm{p}}}}\right)-t_{\mathrm{r}}+t_{\mathrm{f}}\right]+\\
\quad+\dfrac{U_{\mathrm{D}}}{R_0t_{\mathrm{r}}}\left[\dfrac{L_0}{R_0}e^{-\frac{R_0}{L_0}t}\left(1-e^{\frac{R_0}{L_0}t_{\mathrm{r}}}-e^{\frac{R_0}{L_0}(t_{\mathrm{r}}+t_{\mathrm{on}})}+e^{\frac{R_0}{L_0}(t_{\mathrm{r}}+t_{\mathrm{on}}+t_{\mathrm{f}})}\right)+t_{\mathrm{r}}-t_{\mathrm{f}}\right]
\end{cases}
\tag{14}
$$

Although the present analysis focuses on the differential-mode load current, the parasitic capacitance $C_{\mathrm{p}}$ defines the common-mode return path through which leakage and conducted-EMI currents flow. Quantifying this common-mode contribution requires experimental characterization, which is identified as future work.

## 4. State-Space Current-Response Model With a Passive LC Filter

When the load impedance, parasitic capacitance, and passive LC filter are considered simultaneously, the number of coupled energy-storage elements makes direct piecewise Laplace-domain manipulation cumbersome. A state-space representation is therefore adopted for the filtered system shown in Figure 5.

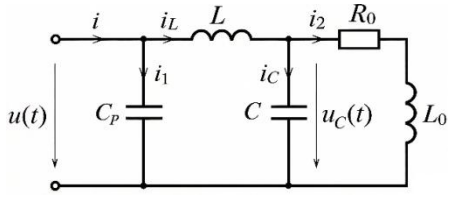


**Figure 5**. Per-phase equivalent circuit including the passive LC filter and the parasitic capacitance $C_{\mathrm{p}}$ .

The state variables are the filter-inductor current $i_L$ , the filter-capacitor voltage $u_C$, and the load current $i_2$ , with the current directions defined in Figure 5. Kirchhoff's current law at the input and filter-capacitor nodes gives $i=i_1+i_L$ and $i_L=i_C+i_2$ , respectively. Applying Kirchhoff's voltage law to the filter loop and the load branch yields the state equations in Eq. (15).

$$
\begin{cases}
\dfrac{\mathrm{d}i_L}{\mathrm{d}t}=\dfrac{1}{L}u-\dfrac{u_C}{L}\\
\dfrac{\mathrm{d}u_C}{\mathrm{d}t}=\dfrac{i_L}{C}-\dfrac{i_2}{C}\\
\dfrac{\mathrm{d}i_2}{\mathrm{d}t}=\dfrac{u_C}{L_0}-\dfrac{R_0}{L_0}i_2
\end{cases}
\tag{15}
$$

Equation (15) is recast in matrix form in equation 16.

$$
\begin{pmatrix}\dfrac{\mathrm{d}i_L}{\mathrm{d}t}\\ \dfrac{\mathrm{d}u_C}{\mathrm{d}t}\\ \dfrac{\mathrm{d}i_2}{\mathrm{d}t}\end{pmatrix}=\begin{pmatrix}0 & -\dfrac{1}{L} & 0\\ \dfrac{1}{C} & 0 & -\dfrac{1}{C}\\ 0 & \dfrac{1}{L_0} & -\dfrac{R_0}{L_0}\end{pmatrix}\begin{pmatrix}i_L\\ u_C\\ i_2\end{pmatrix}+\begin{pmatrix}\dfrac{1}{L} & 0 & 0\\ 0 & 0 & 0\\ 0 & 0 & 0\end{pmatrix}\begin{pmatrix}u\\ 0\\ 0\end{pmatrix}
\tag{16}
$$

where the state vector, input vector, and system matrices are defined in equation 16.

$$\dot{X}=\begin{pmatrix}\frac{\mathrm{d}i_L}{\mathrm{d}t}\\ \frac{\mathrm{d}u_C}{\mathrm{d}t}\\ \frac{\mathrm{d}i_2}{\mathrm{d}t}\end{pmatrix}\quad X=\begin{pmatrix}i_L\\ u_C\\ i_2\end{pmatrix}\quad U=\begin{pmatrix}u\\ 0\\ 0\end{pmatrix}\quad A=\begin{pmatrix}0 & -\frac{1}{L} & 0\\ \frac{1}{C} & 0 & -\frac{1}{C}\\ 0 & \frac{1}{L_0} & -\frac{R_0}{L_0}\end{pmatrix}\quad B=\begin{pmatrix}\frac{1}{L} & 0 & 0\\ 0 & 0 & 0\\ 0 & 0 & 0\end{pmatrix}$$

Using these definitions, the compact state equation becomes equation 17.

$$\dot{X}=AX+BU \quad (17)$$

The state equation is integrated numerically by the classical fourth-order Runge-Kutta method. For a time step $\Delta t$, the state at sample $j+1$ is calculated from equation 18.

$$X\left[(j+1)\Delta t\right]=X(j\cdot\Delta t)+\frac{\Delta t}{6}\left(k_1^j+2k_2^j+2k_3^j+k_4^j\right) \quad (18)$$

with the four Runge-Kutta slope vectors evaluated in equation 18.

$$\begin{aligned}k_1^j &= AX(j\cdot\Delta t)+BU(j\cdot\Delta t)\\ k_2^j &= A\left[X(j\cdot\Delta t)+\frac{\Delta t}{2}\cdot k_1^j\right]+BU\left[(j+\frac{1}{2})\cdot\Delta t\right]\\ k_3^j &= A\left[X(j\cdot\Delta t)+\frac{\Delta t}{2}\cdot k_2^j\right]+BU\left[(j+\frac{1}{2})\cdot\Delta t\right]\\ k_4^j &= A\left[X(j\cdot\Delta t)+\Delta t\cdot k_3^j\right]+BU\left[(j+1)\cdot\Delta t\right]\end{aligned}$$

The same four switching intervals used in the analytical model are imposed on the input voltage $u(t)$. The state vector is advanced step-by-step over each interval, so that the transient branch currents and capacitor voltage can be reconstructed for the complete voltage impulse.

This formulation enables the effects of $L$ and $C$ to be examined without changing the underlying physical description of the switching event.

The RK4 integration time step is $\Delta t=0.1$ μs. A reduction of $\Delta t$ to 0.05 μs produced negligible changes in the results, confirming step-size insensitivity.

## 5. Simulation Setup and Influence of Passive-Filter Parameters

The resonant frequency of each LC configuration is calculated as:

$$f_{\mathrm{r}}=\frac{1}{2\pi\sqrt{LC}} \quad (19)$$

Table 2 summarizes the resonant frequencies for the investigated cases.

**Table 2**. Resonant frequency of each LC configuration.

| Case | $L$ (mH) | $C$ (μF) | $f_{\mathrm{r}}$ (Hz) | $f_{\mathrm{r}}/f_{\mathrm{sw}}$ |
|---|---|---|---|---|
| 1 | 0.03 | 50 | 4109 | 1.71 |
| 2 | 0.03 | 200 | 2054 | 0.86 |
| 3 | 2 | 50 | 503 | 0.21 |

The switching frequency is $f_{\mathrm{sw}}=2.4$ kHz, while the fundamental is $f=60$ Hz. For an output LC filter to be effective, its resonant frequency $f_{\mathrm{r}}$ should be placed sufficiently above the fundamental to avoid loading the power path, and sufficiently below the carrier to ensure attenuation rather than amplification of the switching harmonics. Case 3 ( $f_{\mathrm{r}}=503$ Hz) satisfies both conditions: it lies well above $f_1$ and well below $f_{\mathrm{sw}}$, so the carrier and its sidebands fall inside the −40 dB/decade attenuation band. Case 2 ( $f_{\mathrm{r}}=2054$ Hz) places the resonance close to $f_{\mathrm{sw}}$, where the filter can amplify switching harmonics instead of suppressing them. Case 1 ( $f_{\mathrm{r}}=4109$ Hz) places the resonance above $f_{\mathrm{sw}}$, so the network is already capacitive at the carrier and provides insufficient attenuation. Damping is provided by the load resistance $R_0=5$ Ω; no additional damping network is included in this study. Large $\mathrm{d}u/\mathrm{d}t$ and $\mathrm{d}i/\mathrm{d}t$ values produced by inverter switching act as excitation sources for EMI. The voltage slew rate charges the parasitic capacitances between the semiconductor devices, heat sink, motor windings, and ground, thereby producing common-mode current. The current slew rate simultaneously excites parasitic inductances in the power path and contributes to differential-mode voltage and current oscillations.

Figure 6 shows the inverter-fed motor system used for the numerical study.

The investigated drive consists of a 380 V, 139 A, 60 Hz, 75 kW induction motor supplied by a 130 kVA inverter. The equivalent motor parameters used in the transient model are $R_0=5$ Ω and $L_0=2$ mH. The switching conditions and parasitic-capacitance parameters follow from the system specification summarized in Table 3.

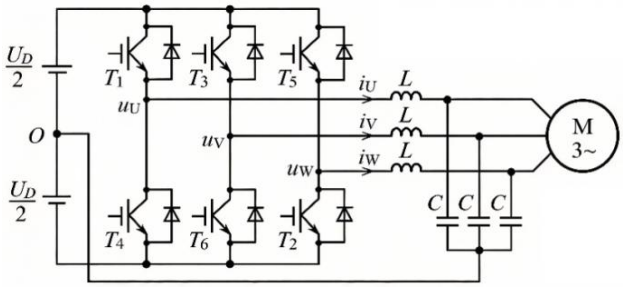


**Figure 6**. Three-phase PWM inverter-fed induction-motor drive system with an output LC filter.

The modulating frequency is 60 Hz, the PWM carrier frequency is 2.4 kHz, and the IGBT rise and fall times are each 0.1 μs.

For the insulating layer between the IGBT and the heat sink, the relative permittivity is $\varepsilon_r = 8.5$, the insulation thickness is $d = 0.03$ cm, and the total heat-sink area is $S_{total} = 63\,\text{cm}^2$. The projected area of a single IGBT on the heat sink is:

$$S_T = \eta \cdot \frac{S_{total}}{6} = 0.75 \cdot \frac{63}{6} = 7.875\,\text{cm}^2 \quad (20)$$

where $\eta = 0.75$ is the effective area coefficient, representing the fraction of the heat-sink area that is effectively coupled to each IGBT through the insulating layer; the division by 6 distributes the total effective area over the six IGBTs of the three-phase bridge. The per-IGBT parasitic capacitance $C_T$ is calculated from the parallel-plate formula:

$$C_T = \varepsilon_0 \varepsilon_r \frac{S_T}{d} \quad (21)$$

where $\varepsilon_0 = 8.854 \times 10^{-12}\ \text{F/m} = 0.0885\ \text{pF/cm}$. Substituting these values into equation 21 yields:

$$C_T = 0.0885 \times 8.5 \times 7.875 / 0.03 = 197.465\,\text{pF} \quad (22)$$

The equivalent capacitance of one phase leg, $C_p$, is given by equation (23), following from the time-averaged three-phase coupling established in Section 3

$$C_p = 2 \times C_T = 2 \times 197.465 = 394.93\,\text{pF} \quad (23)$$

This value is used in the subsequent analysis.

To demonstrate the effect of the parasitic capacitance, the load-current waveforms with and without $C_p$ were compared for the best-performing configuration ( $L = 2$ mH, $C = 50$ μF). The difference in the load-current RMS ripple between the two cases was below 0.01%, confirming that the parasitic branch conducts a negligible fraction of the switching-frequency current. This result is consistent with the reactance ratio: with $C_p = 394.93$ pF and $f_{sw} = 2.4$ kHz, the reactance is $1/(2\pi f_{sw} C_p) \approx 168$ kΩ, which exceeds $R_0 = 5$ Ω by a factor of approximately $3.4 \times 10^4$. The differential-mode load-current waveform is therefore governed by the filter elements $L$ and $C$, while the model retains the common-mode return path through $C_p$ for future EMI assessment.

**Table 3**. Simulation parameters.

| Parameter | Value |
|---|---|
| DC-link voltage $U_D$ | 550 V |
| Fundamental frequency | 60 Hz |
| Switching frequency | 2.4 kHz |
| IGBT rise/fall time | 0.1 μs |
| Load resistance $R_0$ | 5 Ω |
| Load inductance $L_0$ | 2 mH |
| Parasitic capacitance $C_p$ | 394.93 pF |
| RK4 time step $\Delta t$ | 0.1 μs |

Figure 7 shows the calculated load-current waveform without an output filter.

Without filtering, the load current contains visible high-frequency ripple superimposed on the 60 Hz fundamental component. This result establishes the baseline for evaluating the three passive-filter parameter sets.

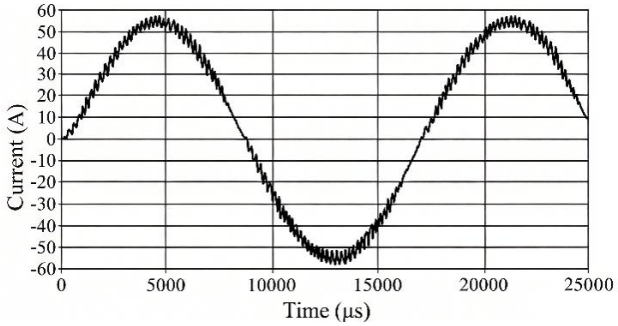


**Figure 7**. Analytical load-current waveform over one switching period (μs scale) without an output filter.

For the first filter case, $L = 0.03$ mH and $C = 50$ μF are used at a 2.4 kHz carrier frequency. Figure 8(a) shows the resulting inverter output current, while Figure 8(b) reveals that the load current remains strongly affected by switching ripple. The corresponding filter-capacitor voltage is shown in Figure 8(c).

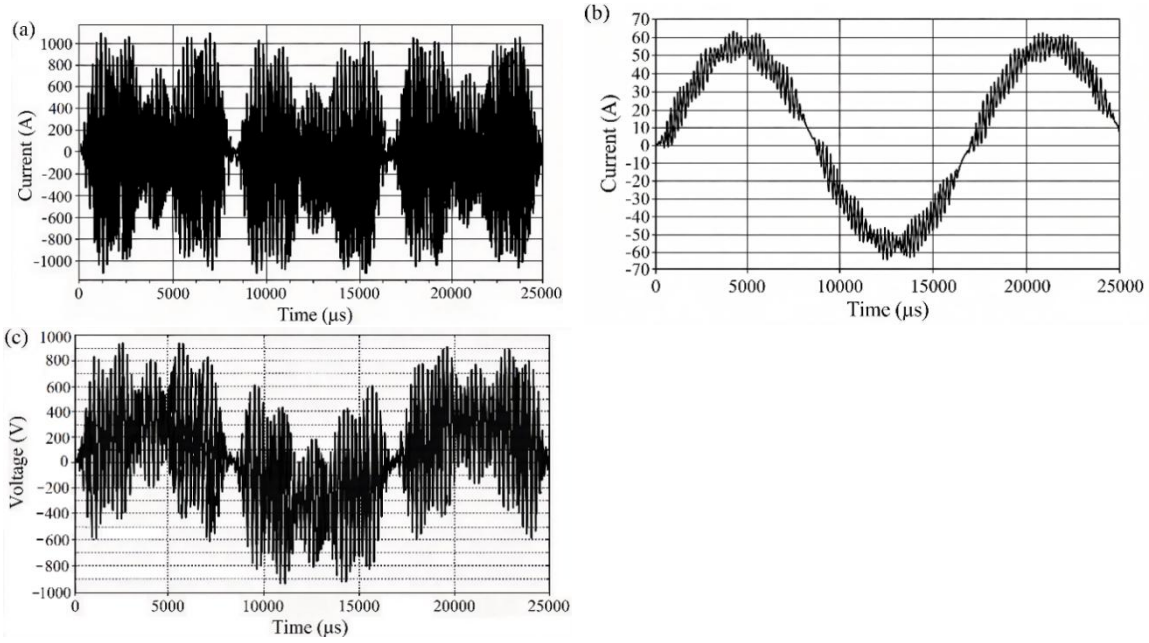


**Figure 8**. Analytical waveforms over one switching period (μs scale) with $L = 0.03$ mH and $C = 50$ μF. (a) Load current, (b) Inverter output current and (c) Filter capacitor voltage.

The small filter inductance provides insufficient attenuation of the switching-frequency current components. Therefore, the presence of an LC network alone does not guarantee satisfactory transient performance; the component values must be chosen with respect to both the switching excitation and the load impedance.

In this case, both the inverter output current and capacitor voltage exhibit large high-frequency excursions. The result illustrates a potentially unfavorable filter condition: an inadequately damped or weakly attenuating LC network can transfer substantial switching stress to the inverter-side current and capacitor voltage instead of effectively isolating the motor from the switching waveform.

Accordingly, filter selection should be based on the combined response of the inverter current, capacitor voltage, and load current rather than on the load-current waveform alone.

The second parameter set increases the capacitance to $C = 200$ μF while retaining $L = 0.03$ mH. Figure 9 shows the inverter output current, capacitor voltage, and load current for this configuration.

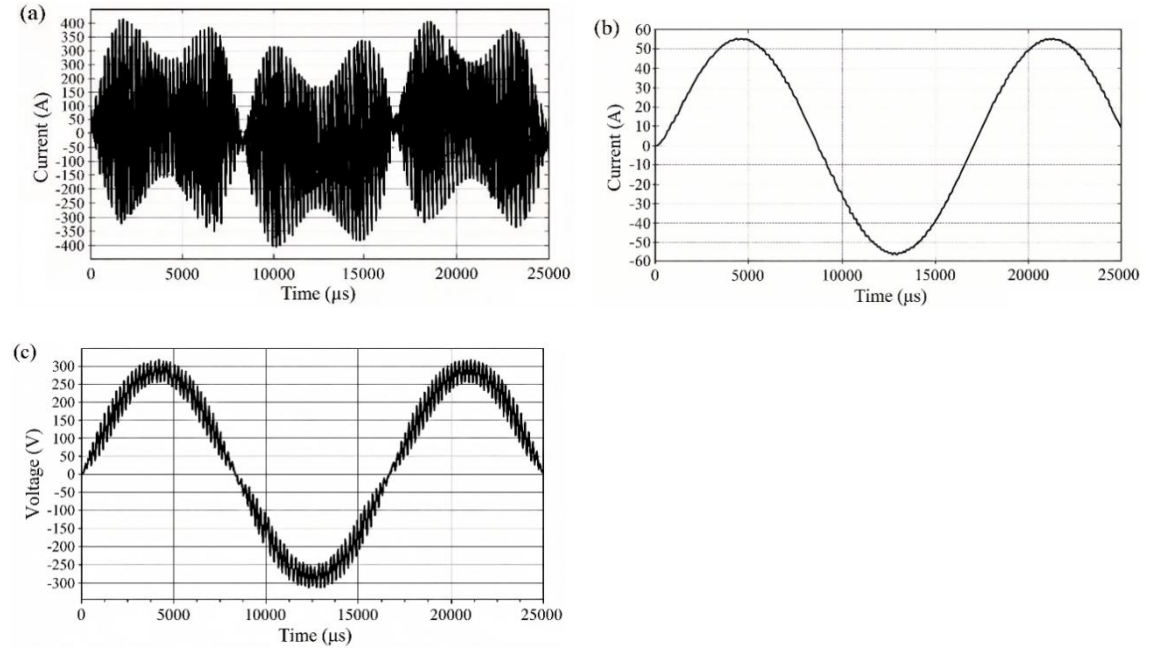


**Figure 9**. Analytical waveforms over one switching period (μs scale) with $L = 0.03$ mH and $C = 200$ μF. (a) Inverter output current, (b) Load current, (c) Filter capacitor voltage.

Increasing the capacitance reduces the inverter-side current excursion relative to the 50 μF case and produces a load-current waveform that is closer to a sinusoid. Nevertheless, residual high-frequency components remain visible, indicating that increasing $C$ alone does not fully control the transient current response when $L$ remains very small.

The third filter case uses $L = 2$ mH and $C = 50$ μF. Figure 10 shows the corresponding inverter output current, load current, and filter-capacitor voltage.

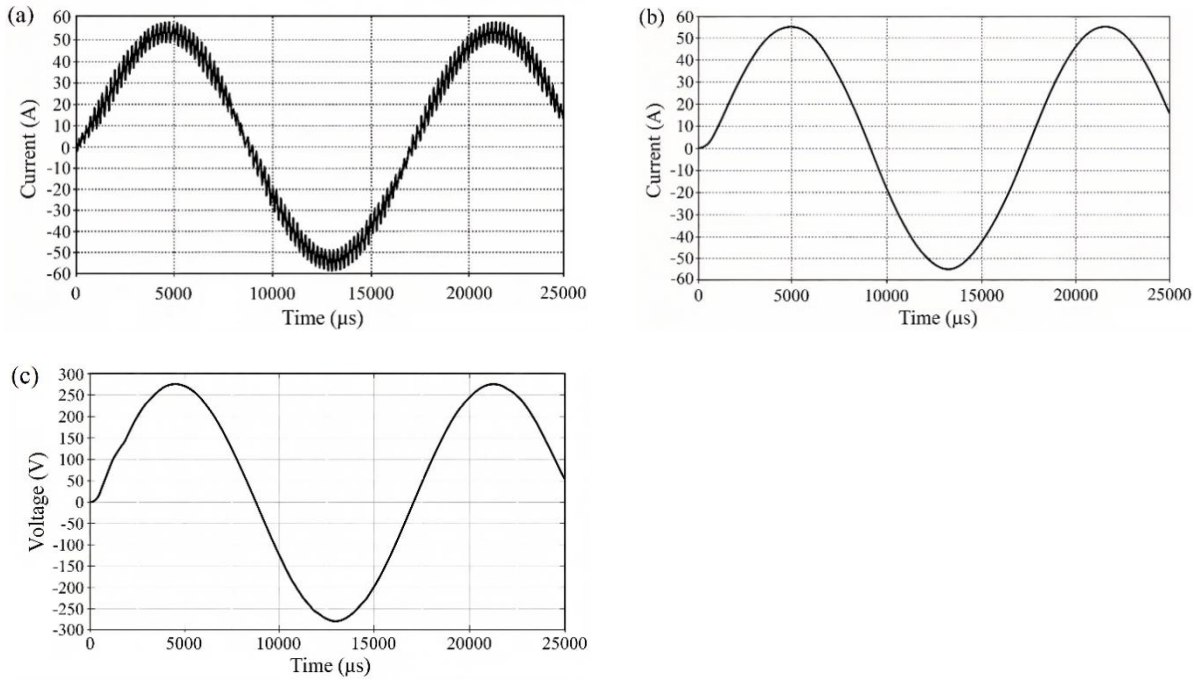


**Figure 10**. Analytical waveforms over one switching period (μs scale) with $L = 2$ mH and $C = 50$ μF. (a) Inverter output current, (b) Load current, (c) Filter capacitor voltage.

Among the investigated parameter sets, $L = 2$ mH and $C = 50$ μF gives the smoothest waveforms. The inverter output current and capacitor voltage show substantially reduced high-frequency oscillation, while the load current is close to the expected sinusoidal fundamental waveform.

The comparison confirms that the filter inductance is particularly important for limiting switching-frequency current excursions. A poorly selected LC combination can leave significant harmonic content in the load current and can also increase the current stress experienced by the inverter switching devices. The proposed transient-response model is therefore useful as a screening tool for candidate passive-filter parameters prior to full-scale experimental qualification.

## 6. Numerical Implementation and Discussion

In this section, the analytical and state-space formulations are implemented numerically in MATLAB, and the resulting waveforms are examined to confirm the internal consistency of the proposed modeling approach. This serves two purposes: (i) to verify that the numerical implementation reproduces the analytical and state-space formulations, and (ii) to provide quantitative performance metrics (load-current THD, peak inverter current, RMS ripple, and attenuation at the switching frequency) that support the qualitative comparisons in Section 5.

The voltage and current responses predicted by the proposed formulation were also evaluated in MATLAB. Figure 11-Figure 13 present the combined inverter output current, load current, and filter-capacitor voltage for the filter configurations considered in the numerical study.

Figure 11 illustrates a weak-filtering condition in which substantial switching-frequency components remain in the inverter current and capacitor voltage while the load current still contains noticeable ripple.

Figure 12 shows the response for $L = 0.03$ mH and $C = 200$ μF. Relative to the weak-filtering case, the inverter-current excursion is reduced and the load current is more sinusoidal, although switching ripple remains in the capacitor voltage.

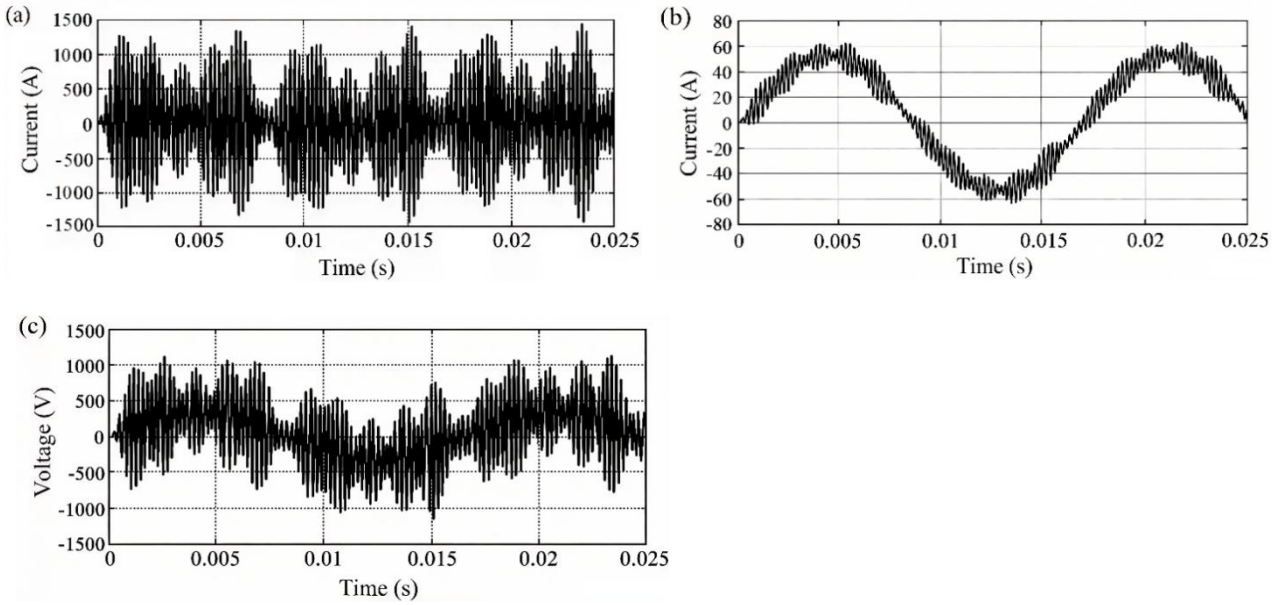


**Figure 11**. MATLAB waveforms for the first verification case. (a) Inverter output current, (b) Load current, (c) Filter capacitor voltage.

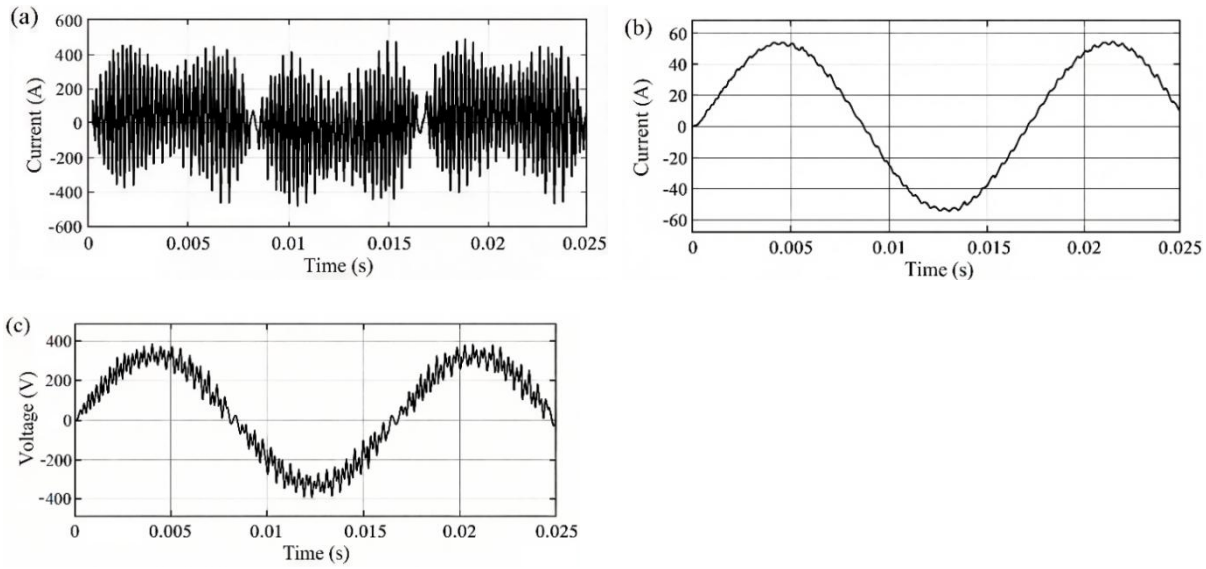


**Figure 12**. MATLAB waveforms obtained with $L = 0.03$ mH and $C = 200$ μF. (a) Inverter output current, (b) Load current, (c) Filter capacitor voltage.

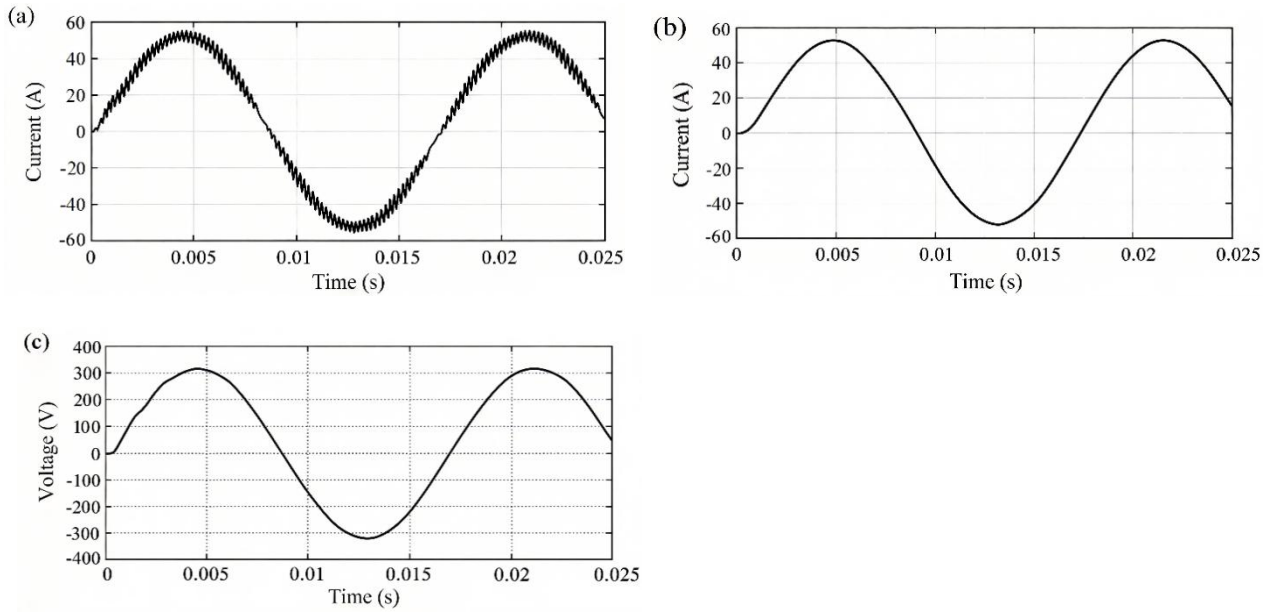


**Figure 13**. MATLAB waveforms with $L = 2$ mH and $C = 50$ μF. (a) Inverter output current, (b) Load current, (c) Filter capacitor voltage.

Figure 13 shows the response for $L = 2$ mH and $C = 50$ μF. This case provides the cleanest load-current waveform and the lowest visible inverter-side high-frequency oscillation among the compared cases, supporting the qualitative trend obtained from the current -response analysis in Section 5.

To provide a quantitative basis for the comparison, four metrics were calculated for each configuration: the load-current THD, the peak inverter current, the root-mean-square (RMS) ripple, and the attenuation at the switching frequency. These values are summarized in Table 4. The configuration $L = 2$ mH and $C = 50$ μF yields the lowest simulated load-current THD (2.3%) and the highest attenuation at the switching frequency (38.4 dB), consistent with the waveform comparison in Figure 8-Figure 12. The THD values were obtained via FFT analysis of the load-current waveforms over the steady-state fundamental period (0.02-0.025 s); the peak and RMS values were extracted directly from the time-domain waveforms.

**Table 4**. Quantitative comparison of filter configurations (simulation-derived).

| | Load-current THD (%) | Peak inverter current (A) | RMS ripple (A) | Attenuation at switching-frequency (dB) |
|---|---|---|---|---|
| No-filter | 28.6 | 1050 | 42.3 | 0 (reference) |
| Case 1 | 18.4 | 980 | 35.7 | 8.2 |
| Case 2 | 9.7 | 410 | 18.5 | 19.6 |
| Case 3 | 2.3 | 60 | 3.1 | 38.4 |

The present study focuses on the differential-mode transient current response and filter parameter screening. Quantitative common-mode current, leakage current, and conducted-EMI spectra are beyond the scope of the current simulation framework and will be addressed in future experimental work using a line-impedance stabilization network and high-bandwidth current probes.

## 7. Conclusion

This paper presented a transient current-response framework for three-phase PWM inverter systems excited by finite-rise-time voltage impulses. The model was developed progressively for three levels of complexity: an R-L load, a load including the dominant heat-sink-related parasitic capacitance, and a passive-LC -filtered inverter represented in state-space form. Laplace -domain convolution yields closed-form piecewise current expressions for the first two cases, whereas a fourth-order Runge-Kutta procedure is used for the filtered system. Application to a 380 V, 75 kW induction -motor drive shows that the passive-filter parameters strongly affect the inverter output current, filter-capacitor voltage, and load-current ripple; among the investigated combinations, $L = 2$ mH and $C = 50$ μF gives the smoothest waveforms and the lowest simulated THD. The heat-sink parasitic capacitance was quantified as 394.93 pF and shown to carry negligible current at the

carrier frequency, so the differential-mode result is governed by the filter elements, while the model retains the common-mode return path for future EMI assessment. The main value of the proposed method is that it links the switching-voltage impulse directly to the transient differential-mode current paths, providing a physics-based foundation for screening passive EMI-filter parameters before prototype testing. Full experimental and EMC qualification—including LISN measurements, high-bandwidth current probing, and motor-bearing and ground-current measurement—remains necessary to validate the differential-mode current model and quantify common-mode and conducted-EMI metrics.


## Acknowledgments

Not applicable.


## Data Availability

The data supporting the findings of this study are available from the corresponding author upon reasonable request.

## Ethics Statement

Not applicable.

## AI Statement

The authors declare that no generative AI tools were used in the preparation of this manuscript.

## Declaration of Competing Interest

The authors declare that they have no known competing financial interests or personal relationships that could have appeared to influence the work reported in this paper.

## CRediT Authorship Contribution Statement

YunHo Pak: Conceptualization, Methodology, Formal analysis, Investigation, Writing-original draft. JuSong Kim: Software, Validation, Data curation, Visualization. YongSim Ro: Resources, Supervision, Project administration. JinHyok Ri: Conceptualization, Methodology, Writing-review & editing, Corresponding author.


## Funding

This research did not receive any specific grant from funding agencies in the public, commercial, or not-for-profit sectors.


## References


[1] M.M. Swamy, K. Yamada, T. Kume. Common mode current attenuation techniques for use with PWM drives. IEEE Transactions on Power Electronics, 2001, 16(2), 248-255. DOI: 10.1109/63.911149

[2] S. Ogasawara, H. Akagi. Modeling and damping of high-frequency leakage currents in PWM inverter-fed AC motor drive systems. IEEE Transactions on Industry Applications, 1996, 32(5), 1105-1114. DOI: 10.1109/28.536872

[3] F. Wang. Motor shaft voltages and bearing currents and their reduction in multilevel medium-voltage PWM voltage-source-inverter drive applications. IEEE Transactions on Industry Applications, 2000, 36(5), 1336 -1341. DOI: 10.1109/28.871282

[4] A.K. Morya, M.C. Gardner, B. Anvari, L.M. Liu, A.G. Yepes, J. Doval-Gandoy, et al. Wide bandgap devices in AC electric drives: Opportunities and challenges. IEEE Transactions on Transportation Electrification, 2019, 5(1), 3-20. DOI: 10.1109/TTE.2019.2892807

[5] T.G. Habetler, R. Naik, T.A. Nondahl. Design and implementation of an inverter output LC filter used for dv/dt reduction. IEEE Transactions on Power Electronics, 2002, 17(3), 327-331. DOI: 10.1109/TPEL.2002.1004240

[6] H. Akagi, H. Hasegawa, T. Doumoto. Design and performance of a passive EMI filter for use with a voltage -source PWM inverter having sinusoidal output voltage and zero common-mode voltage. IEEE Transactions on Power Electronics, 2004, 19(4), 1069-1076. DOI: 10.1109/TPEL.2004.830039

[7] H. Akagi, T. Doumoto. A passive EMI filter for preventing high-frequency leakage current from flowing through the inverter heat sink of an adjustable-speed motor drive system. Conference Record of the 2004 IEEE Industry Applications Conference, 39th IAS Annual Meeting, 2004, 3, 2003-2009. DOI: 10.1109/ias.2004.1348743

[8] P. Pairodamonchai, S. Suwankawin, S. Sangwongwanich. Design and implementation of a hybrid output EMI filter for high-frequency common-mode voltage compensation in PWM inverters. IEEE Transactions on Industry Applications, 2009, 45(5), 1647-1659. DOI: 10.1109/TIA.2009.2027352

[9] K. Jayaraman, M. Kumar. Design of passive common-mode attenuation methods for inverter-fed induction motor drive with reduced common-mode voltage PWM technique. IEEE Transactions on Power Electronics, 2020, 35(3), 2861-2870. DOI: 10.1109/TPEL.2019.2930825

[10] Y.C. Zhang, Q. Li, D. Jiang. A motor CM impedance based transformerless active EMI filter for DC-side common-mode EMI suppression in motor drive system. IEEE Transactions on Power Electronics, 2020, 35(10), 10238-10248. DOI: 10.1109/TPEL.2020.2980881

[11] N. Jia, X.Y. Tian, L.X. Xue, H. Bai, L.M. Tolbert, H. Cui. In-package common-mode filter for GaN power module with improved radiated EMI performance. 2022 IEEE Applied Power Electronics Conference and Exposition, 2022, 974-979. DOI: 10.1109/APEC43599.2022.9773764

[12] N. Jia, X.Y. Tian, L.X. Xue, H. Bai, L.M. Tolbert, H. Cui. Integrated common-mode filter for GaN power module with improved high-frequency EMI performance. IEEE Transactions on Power Electronics, 2023, 38(6), 6897-6901. DOI: 10.1109/TPEL.2023.3248092

[13] W.Z. Zhou, X.B. Yuan, Z.B. Zhang. An active dv/dt filter to combat motor terminal overvoltage in SiC-based adjustable speed drives. IEEE Transactions on Industrial Electronics, 2025, 72(1), 1076-1081. DOI: 10.1109/TIE.2024.3406874

[14] S. Takahashi, R. Kanbayashi. Passive cancellation of input and output common-mode noise in three-phase PWM inverter-fed motor drive systems. IEEJ Journal of Industry Applications, 2025, 14(3), 442-449. DOI: 10.1541/ieejjia.24009161

[15] S. Wang, Y.Y. Maillet, F. Wang, D. Boroyevich, R. Burgos. Investigation of hybrid EMI filters for common-mode EMI suppression in a motor drive system. IEEE Transactions on Power Electronics, 2010, 25(4), 1034-1045. DOI: 10.1109/TPEL.2009.2033601

[16] Z.L. Zhang, Y.H. Hu, X. Chen, G.W. Jewell, H. Li. A review on conductive common-mode EMI suppression methods in inverter fed motor drives. IEEE Access, 2021, 9, 18345-18360. DOI: 10.1109/ACCESS.2021.3054514

[17] L. Chen, Q.J. Hu, T.Y. Wang, J.W. Qin, K.L. Tan, L. Yang, et al. Conducted electromagnetic interference mechanisms and mitigation techniques in SiC electric vehicle traction inverters: A review. Machines, 2026, 14(9), 1068. DOI: 10.3390/machines14091068

[18] J. Aigner, M. Lemke, T. Dörlemann, S. Frei. Broadband active common mode EMI suppression of a GaN motor inverter with adaptive FIR filters using delay-compensated gate control signals. IEEE Transactions on Electromagnetic Compatibility, 2025, 67(4), 1213-1227. DOI: 10.1109/TEMC.2025.3582516

[19] N. Jia, L.M. Tolbert, H.H. Cui. EMI filter integration for GaN power module using air-cured magnetic composite. 2023 IEEE Energy Conversion Congress and Exposition, 2023, 5684-5691. DOI: 10.1109/ECCE53617.2023.10362742

[20] S. Sundeep, J.B. Wang, A. Griffo. A passive filter for mitigating neutral-point voltage stress in inverter-fed drives. IEEE Transactions on Energy Conversion, 2025, 40(2), 1388-1399. DOI: 10.1109/TEC.2024.3514136